Thermonuclear burn characteristics of compressed deuterium-tritium microspheres ⊘

G. S. Fraley; E. J. Linnebur; R. J. Mason; ... et. al

Check for updates

CrossMark

View Online

Export Citation

Articles You May Be Interested In

Abstract: Tritium diffusion in ceramic materials for thermonuclear reactors

Journal of Vacuum Science and Technology (January 1976)

Tritium permeation and inventory in an international thermonuclear experimental reactor divertor

Journal of Vacuum Science & Technology A (January 1997)

Physics Problems of Thermonuclear Reactors

AIP Conference Proceedings (April 1974)

AIP Publishing

Thermonuclear burn characteristics of compressed deuterium–tritium microspheres

G. S. Fraley, E. J. Linnebur, R. J. Mason, and R. L. Morse

Los Alamos Scientific Laboratory, University of California, Los Alamos, New Mexico 87544

The phenomenology of thermonuclear burn in deuterium–tritium microspheres at high densities is described, and numerical results characterizing the burn for a broad range of initial conditions are given. The fractional burnup, bootstrap-heating, and depletion of the DT fuel, its expansive disassembly, and thermonuclear ignition by propagating burn from central hot spots in the microspheres are discussed. Extensive numerical results from a 3 T Lagrangian simulation code are presented. The yields Y_0 from uniform 10, 1, and 0.1 μg microspheres with densities $\rho = 1$ to 4×10^4 g/cm^3 and temperatures $T_e = T_i = 1.8$ to 100 keV are given. It is shown that $Y_0 \sim \rho R$, $\rho R < 0.3$ (R is the microsphere radius) or, equivalently, $Y_0 \sim \rho^{2/3}$ for spheres of fixed mass m. The gain-factor $G_0 \equiv Y_0/mI_0$ (I_0 is the internal energy) is shown to measure burn efficiency in uniform microspheres. More than a four-fold increment in the gain factor is shown to derive from apportionment of the internal energy in a central hot spot. The limiting effects of electron degeneracy on the gain factor are outlined. As a guideline, the experimental observation of 10^{13} neutrons/kJ of input laser energy is established as proof of good absorption; 10^{15} /kJ will imply yields exceeding break even.

I. INTRODUCTION

Computer simulations[1] indicate that a laser-driven ablative implosion scheme[2] may suffice to compress the inner regions of small DT spheres and shells to extreme densities and temperatures, such that net thermonuclear energy is produced prior to the expansive disassembly of these targets. Details of the thermonuclear burn in DT microspheres at high density therefore become of interest. From a comprehensive understanding of the burn phenomenology, it should be possible to designate the conditions which the implosion scheme must establish for efficient burn of the DT fuel, and the degree to which it is permissible to deviate from these conditions. With this motivation, in this paper, we present results from extensive simulation studies of the burnup and disassembly of microspheres for a broad range of masses, initial densities, and temperatures. We emphasize the effects of localized bootstrap heating, and propagating burn from central hot spots.

Similarity solutions[3,4] and numerical treatments[5] for the disassembly of laser irradiated targets have been available in the literature for some time. However, these papers ignore thermonuclear burn. Recently, Johnson and Hall[6] have calculated the yield from expanding solid density pellets. Their similarity treatment applies if both bootstrap heating and fuel depletion are negligible during the burn.

Calculations for our high density study were performed with the one-dimensional Lagrangian hydrodynamics code used for Ref. 1. It allows for separate ion, electron, and radiation temperatures (a Planckian spectrum for the radiation is assumed). The code employs classical conductivities[7] for the electrons and ions, and classical coupling rates between the electron and ion temperature fields. It accounts for Compton and inverse-Compton scattering, and bremsstrahlung and inverse-bremsstrahlung between the electrons and the radiation

field. It calculates the energy released from D–T and competing D–D nuclear reactions, accounting for time-dependent, nonlocal α-particle energy deposition into the electrons and ions. The computations utilize tabular, Fermi–Thomas–Dirac equations of state, including the effects of electron Fermi-degeneracy on the pressure, internal energy, and opacity of the equimolar DT fuel. Auxiliary calculations were carried out with a separate nonequilibrium Lagrangian code that does Monte Carlo radiation and reaction product particle transport, to provide a cross check on our results. We report good agreement between the two sets of calculations.

The utility of high compression for enhancing the rate of energy release in systems undergoing nuclear reactions was recognized at Los Alamos as early as 1943.[1] Its use in laser fusion had to await the development of powerful short-pulse lasers, such as are now under construction at Los Alamos and Livermore. Reference 1 provided a quantitative picture of the performance anticipated from DT targets exposed to highly optimized laser pulses. Here, we look more closely at the interactive hydrodynamics and thermonuclear chemistry that follow from high compression. In Sec. II, we justify the choice of initial conditions inspected. Section III outlines the pertinent aspects of burn physics, introducing the concept of spherical propagating burn waves. Section IV collects and summarizes the results of more than 800 numerical simulation runs (each requiring, typically, 30 min of CDC 6600 CPU time). Finally, Sec. V relates our results to the predictions of Ref. 1. Also, it establishes guidelines—estimates of likely neutron production from laser irradiated targets—which should help to gauge the success of early laboratory experiments.

II. INITIAL CONDITIONS

Our choice of initial conditions was guided by the optimized implosion results of Ref. 1. There, it was

suggested that a laser input energy of 0.7 kJ/μg of DT was required for good yields, and that, typically, the final compressed pellet core represented ~10% of the original pellet mass. Thus, 2 kJ were required for a 3-μg pellet, of which the inner ~0.3-μg were brought to burn conditions. Consequently, we have studied the burn in 10 μg, 1 μg, and 0.1 μg microspheres, corresponding to laser inputs of 65, 6.5, and 650 J, respectively. The latter energies are consistent with the 10-kJ per nsec-pulse lasers anticipated for the near future.[8]

In the Ref. 1, 3-μg pellet implosion, a core density above 10^4 g/cm^3 was calculated. The present simulations, therefore, went to 4×10^4 g/cm^3. In solid density DT, the energy gain from nuclear reactions exceeds the bremsstrahlung loss[9] when the electrons and ions are above 4-keV temperatures—provided that the α-particle reaction products are recaptured by the plasma; so our runs were made at 3 keV and higher. At $\rho R > 1$ (for example, $\rho > 3000$ g/cm^3 in the 1-μg microsphere), it was found that inverse bremsstrahlung lowered the ignition requirements, so a few calculations were made down to 1.8 keV. In the optimized implosion scheme, high temperatures in the pellet cores were first achieved hydrodynamically by the collapse of overtaking, coalescing shocks just outside the center. This process typically produces 10 to 15-keV central temperatures, which subsequently initiate the thermonuclear burn. Thus, 20 keV was the maximum initial temperature chosen for most of our runs, although a few were made with temperatures as high as 100 keV to observe the consequences of the drop-off in the DT reaction cross section[10] $\langle \sigma v \rangle$ beyond $T_i = 65$ keV. Generally, we started with the electron and ion temperature equal i.e., $T_e = T_i \equiv T$ and with the initial radiation temperature T_r at 1 keV. For simplicity, we restricted our propagation study to burn initiated by 10-keV hot spots in a 1-keV ambient background.

III. PHENOMENOLOGY

A. Burn-up

DT burn is characterized by the reaction time $\tau_r = 1/(n\langle \sigma v \rangle)$. The fuel is consumed in accordance with the burn-up equation[11]

$$\frac{df_r}{dt} = (1 - f_r)^2 \frac{1}{2\tau_r},\qquad(1)$$

in which $f_r \equiv (n_\alpha + n_n)/(n_D + n_T + n_\alpha + n_n)$, or equivalently, $f_r \equiv Y/(326\ m)$, Y being the yield in kJ and m being the pellet mass in μg. Equation (1) describes the progress of the reaction $D + T \to n + \alpha$, in which the neutron is given 14 MeV and the α particle, 3.5 MeV. With a constant τ_r, Eq. (1) has the solution

$$f_r(t) = \frac{t/2\tau_r}{1 + t/2\tau_r} \sim \begin{cases} t/2\tau_r, & t \ll \tau_r \qquad\text{(2a)} \\ 1 - \dfrac{2\tau_r}{t}, & t \gg 2\tau_r. \qquad\text{(2b)} \end{cases}$$

At large times, $t \gg 2\tau_r$, the fuel is strongly depleted, being mostly burned to α's and neutrons. From Eq. (2b), we see that the asymptotic rate of burn-up goes as $(\tau_r/t)^2$.

Bootstrap heating occurs when temperatures in the burning regions of a pellet are raised by redeposition of the α-particle reaction energy. In our simulations, the energy of the α particles generated in the DT fusion reaction is deposited along their path length by Coulomb collisions (see Longmire[12]). The range energy relationship is approximately

$$\frac{dU}{dx} = -23.2\left(\frac{\rho}{\rho_0}\right)\frac{U^{1/2}}{T_e^{3/2}}\left\{1 + 0.17 \ln\left[T_e\left(\frac{\rho_0}{\rho}\right)^{1/2}\right]\right\}$$

$$-0.047\left(\frac{\rho}{\rho_0}\right)\frac{1}{U}\left\{1 + 0.075 \ln\left[T_e^{1/2}\left(\frac{\rho_0}{\rho}\right)^{1/2} U^{1/2}\right]\right\},\qquad(3a)$$

where T_e, the electron temperature, is in keV, $U = E_\alpha/3.5$ meV (E_α is the α energy), and ρ_0 is the solid DT density, 0.213 g/cm^3. The first term represents energy deposited in electrons; the second represents the energy deposited in DT ions. From Eq. (3a) it can be seen that when $U = 1$ and T_e is a few tens of kilovolts, the electron term dominates. However, as U decreases along a trajectory, the ion term eventually dominates. In fact, for these lower values of T_e, exact integrations show the energy deposition rate falling gradually along a trajectory and then rising sharply near the end. Useful estimates of the α range under different conditions can be obtained by integrating Eq. (3a) first with just the electron term, neglecting the ion term, and then with just the ion term. The resulting ranges are, respectively, in centimeters,

$$\lambda_{\alpha e} = A T_e^{3/2}/\rho,$$

$$A = 0.086\ \rho_0\left\{1 + 0.17 \ln\left[T_e\left(\frac{\rho_0}{\rho}\right)^{1/2}\right]\right\}^{-1}\qquad(3b)$$

and

$$\lambda_{\alpha i} = B/\rho,$$

$$B = 10.65\ \rho_0\left\{1 + 0.075 \ln\left[T_e^{1/2}\left(\frac{\rho_0}{\rho}\right)^{1/2}\right]\right\}^{-1}.\qquad(3c)$$

The coefficients A and B are relatively slowly varying functions of ρ and T_e. The correct range, which is less than either Eq. (3b) or (3c), is approximately given by Eq. (3b) at small T_e and by (3c) at large T_e. In all of these estimates, we have assumed that the α velocity is less than the electron thermal velocity, which requires that $T_e > 1$ keV. Also, U was set equal to one in Eq. (3c). It should be noted that when the ion term is strong, there is also significant *scattering* of the α particles, so that the range calculated from Eq. (3a) is only an upper limit on the distance between the point of origin of an α and the end point of its trajectory.

An expression equivalent to Eq. (3a) has been integrated numerically, giving the results plotted in Fig. 1. For this integration, separate terms were used for the energy deposition into the deuterons and tritons, and the $\ln(U^{1/2})$ term was approximated by $[\ln(1) + \ln(T_e^{1/2})]/2 = 0.5 \ln(T_e^{1/2})$. When U dropped to T_e, the remaining α energy was given to the ions. We find that a good fit to the computed range results for $\rho = 0.213$ g/cm^3 is

$$\rho\lambda_\alpha = \frac{1.5 \times 10^{-2}\ T_e^{5/4}}{1 + 8.2 \times 10^{-3}\ T_e^{5/4}}(\text{g/cm}^2)\qquad(3d)$$

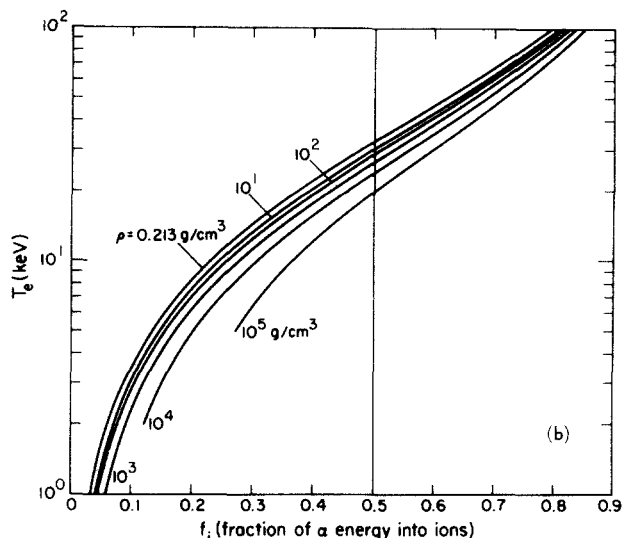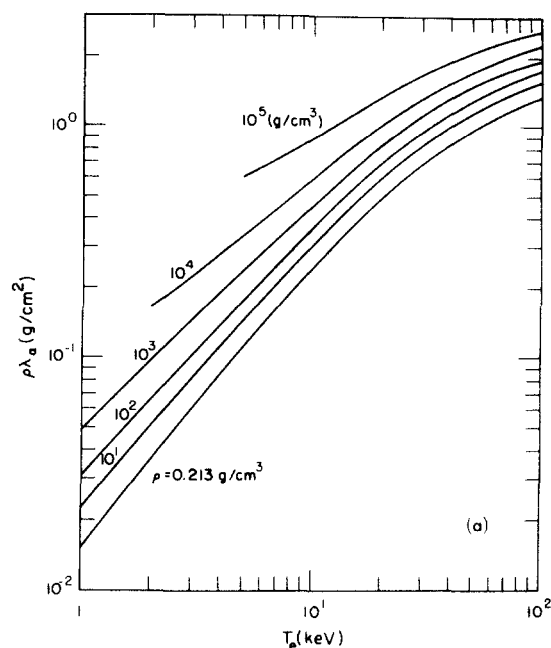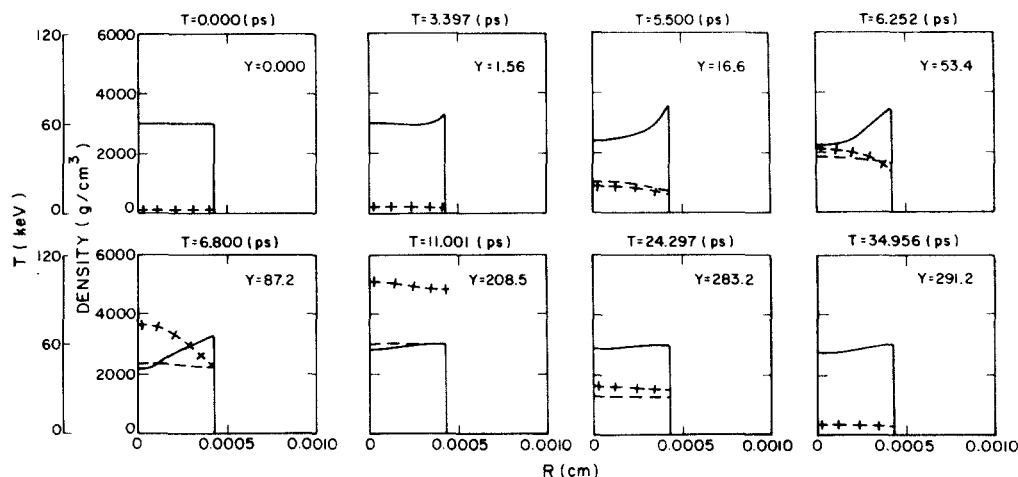FIG. 1. (a) α particle range λ_α vs T_e, (b) α energy absorption.

FIG. 2. Burn-up of a 1-μg sphere with a fixed outer boundary; ρ = 3000 g/cm³, T = 3 keV. T_i + + +, T_e — — —. Evident bootstrap heating.

(accurate to ~2% for T_e from 1 to 100 keV.) Above 10 keV, as ρ goes from solid density to 10^4 g/cm³, the range is increased by roughly a factor $\delta(\rho)$ = 1 → 3 by the Coulomb logarithmic terms. Thus, in proportion to the radius R of a microsphere,

$$\frac{\lambda_\alpha}{R} = \frac{1.9\delta(\rho)}{(1 + 122/T_e^{5/4})} \Big/ \rho R.$$ (3e)

As T_e rises, an increasingly larger fraction f_i of the total α energy is absorbed by the ions. The temperature at which the ions and electrons absorb equal fractions is T_e = 32 keV at solid density, for which the simple rule

$$f_i = \frac{1}{1 + 32/T_e}$$ (4)

agrees with the Fig. 1(b) results from integration to 2% for T_e > 6 keV. With increased ρ, the logarithmic terms reduce the equipartition temperature so·that at 10^4 g/cm³, f_i = 0.5 at only T_e = 24 keV.

In the simulations with our equilibrium code, nonlocal,

time-dependent α-particle energy transport was carried out using Eq.(3a), in an S_n treatment,[13] (Ref. 14, p. 244) employing 6 (and 12) energy groups, with n = 2 in most cases (and n = 4 in a few to test accuracy). In the nonequilibrium code, used as a cross check, the transport was accomplished by a Monte Carlo scheme accounting for the Eq. (3a) energy loss to Coulomb drag.

In uniformly burning spheres, the centers capture the energy preferentially. The edges encounter α's only from the interior; the center "sees" an isotropic source distribution. Figure 2 describes the burn-up of a sphere which has its boundary artificially fixed; i.e., an infinite confinement time applies. Initially, T = 3 keV, m = 1 μg, ρ = 3000 g/cm³, and thus ρR = 1.28. Note that ρR vs ρ plots are provided in Fig. 3; also, from Fig. 1(a) [or Eq. (3e)], λ_α /R = 0.13, so effective α recapture should be evident. The relative mean-free-path for photons[7] (at the average photon energy) is

$$\lambda_p/R = \frac{1.3 T_e^{7/2}(\text{keV})}{\rho} \Big/ \rho R = 1.7 \times 10^{-2}$$ (5)

so inverse bremsstrahlung retards the photon loss from

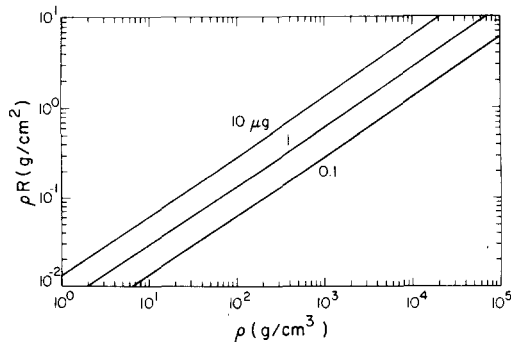FIG. 3. ρR vs ρ for spheres of 10, 1, and 0.1 μg.

the microsphere, T_e remains up, and the fuel ignites at 3 keV. At first, $t < 5$ psec, electron heating is favored. But by $t = 6.252$ psec, $T_e > 32$ keV at the center. Then, T_i can surpass T_e and rise to over 100 keV. The preferential central heating and the need for pressure balance produce a significant depression of density in the middle of the microsphere during the first 10 psec. Thereafter, fuel depletion, in accordance with Eq. (1) (for an appropriate mean τ_r), significantly reduces the energy production rate. The ion thermal energy couples into the electrons, and then into the radiation field. After 35 psec, the burn is quenched, since the net energy loss through radiation exceeds the depleted production rate. Of the 326 kJ ideally available from the DT microgram, only 291 kJ are released.

B. Disassembly

In the case of a free boundary, the first expansion wave signaling disassembly reaches the center of the sphere in a time R/C_s, where $C_s = [(\gamma_i P_i + \gamma_e P_e)/\rho]^{1/2}$ is the speed of sound. Generally, $\gamma_i = \gamma_e = \frac{5}{3}$. But in some cases, the high electron conductivity can make the electrons isothermal, i.e., effectively $\gamma_e = 1$. Alternatively, bootstrap heating can make $P_i \gg P_e$, and heightened ion conductivity can produce the tendency $\gamma_i \to 1$. Thus, at high temperatures, in the extreme, $C_s \to (P_i/\rho)^{1/2} = (T_i/m_i)^{1/2} = V_{th}$, but most often $C_s \to \sqrt{10/3}V_{th}$.

As temperature is decreased, on the other hand, there is a minimum pressure

$$P_e = nT_{ef}\left[1 + \frac{\pi^2}{15}(T_e/T_{ef})^2 + \cdots\right] \quad (keV/cm^3) \quad (6)$$

consistent with the Fermi degeneracy of the electrons. As usual, $\varepsilon_f = (h^2/2m_e)(\frac{3}{8}n_e)^{2/3}$, while here we have defined an "equivalent Fermi temperature" $T_{ef} \equiv \frac{2}{3}\varepsilon_f$, such that $\frac{3}{2}T_{ef} = \frac{3}{5}\varepsilon_f$—the mean kinetic energy of electrons in the limit of full degeneracy[15] ($T_e \to 0$). For DT,

$$T_{ef}(keV) = 5.65 \times 10^{-3}\rho^{2/3} \quad (g/cm^3); \quad (7)$$

T_{ef} is 2 eV at solid density, and 0.94 keV at $10^4 \times$ solid. For T_e near T_{ef} the degeneracy "floor" on P_e must force more rapid disassembly than anticipated classically. At $\rho = 10^4$ g/cm^3, for example, $T_{ef} = 3.6$ keV so that at $T_e = 1$ keV, Eq. (6) gives a pressure ~ 2.9 times greater than the usual $P_e = n_e T_e$.

The outer half-radius of a sphere contains 88% of its mass and, on the average, only half the mass in a given

ΔR is burning while the expansion wave is crossing. These effects reduce the effective disassembly time to $\tau_e = R/4C_s$. That is, for a sphere, the mean burning mass to time $t = R/C_s$ is

$$\langle m(t)\rangle = \frac{\int_0^{t=R/C_s} \frac{4\pi\rho}{3}(R - C_s t)^3 dt}{R/C_s} = \frac{m(t = 0)}{4},$$

and, since $\tau_e m(t = 0) \equiv \langle m(t)\rangle/C_s$, $\tau_e = R/4C_s$.

We define f_{r0} and Y_0 as the fractional burn-up encountered and the yield produced in the full disassembly of initially uniformly heated microspheres. We can use τ_e in (2a) to predict f_{r0} and Y_0, provided the initial density and temperature are low enough so that there is only negligible fuel depletion and bootstrap heating. Thus, for $\tau_e \ll 2\tau_r$, we get

$$f_{r0} = \frac{\tau_e}{2\tau_r} = \left(\frac{\langle\sigma v\rangle}{8C_s m_i}\right)\rho R, \quad (8a)$$

and

$$Y_0 = D\rho R, \quad D = \frac{326m\langle\sigma v\rangle}{8C_s m_i}, \quad (8b)$$

so that for a family of microspheres of fixed mass m and different initial densities

$$Y_0 = E\rho^{2/3}, \quad E = (3m/4\pi)^{1/3}D. \quad (8c)$$

Figure 4 shows the burning of the Fig. 1 1-μg sphere when its outer boundary is free. There is minimal bootstrap heating, T has risen from 3 to 4 keV by 3 psec, and by 6 psec most of the yield (only 0.7 kJ) is out. By this same time, the infinitely confined system had heated to 40 keV, with a large reduction in T_i, and with 50 kJ released. Figure 5 shows how the yield improves in the free system when we start at 20 keV. The long interval for bootstrapping is avoided, so that by 2.1 psec, we have the Fig. 2 energy output to 3.3 psec. By 3.4 psec, however, expansion has terminated the burn. Note that in Fig. 5, T_i first exceeds T_e at $t = 0.83$ psec when the central $T_e = 40$ keV, in agreement with Eq. (4). Note also that the flat T_e profiles in the low-density exterior of the pellet derive from the high electron thermal conductivity operating there.

C. Energy gain

At high density ($\rho R > 1.0$), the microspheres will ignite at 3 keV by virtue of inverse bremsstrahlung, as demonstrated by Figs. 2 and 4. But at 10–20 keV, the yield is significantly improved by circumventing the bootstrap-heating time. Going higher in temperature is not helpful, since between 20 and 70 keV the yields are nearly constant with only a slight peak at 40 keV, the ($\langle\sigma v\rangle/C_s$) maximum. In any case, high temperatures require greater laser input energy. At nondegenerate densities, DT has the specific internal energy,

$$I = I_i + I_e$$
$$= 5.8 \times 10^{-2}[T_i(keV) + T_e(keV)] \quad (kJ/\mu g). \quad (9)$$

In practice, we will want to optimize the gain factor

$$G_F = Y/mI. \quad (10a)$$

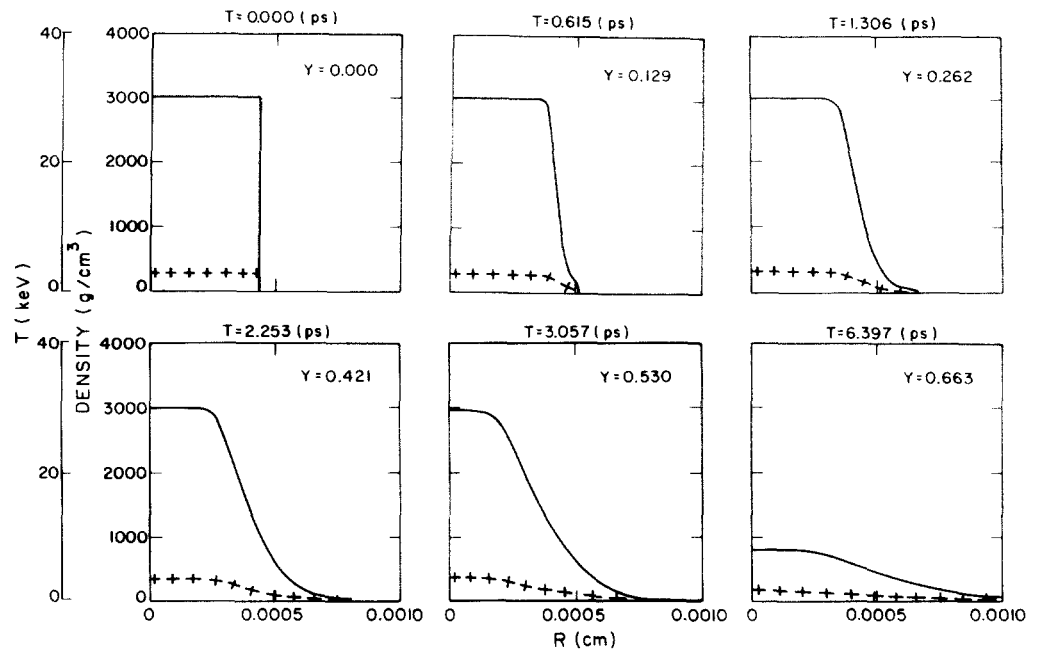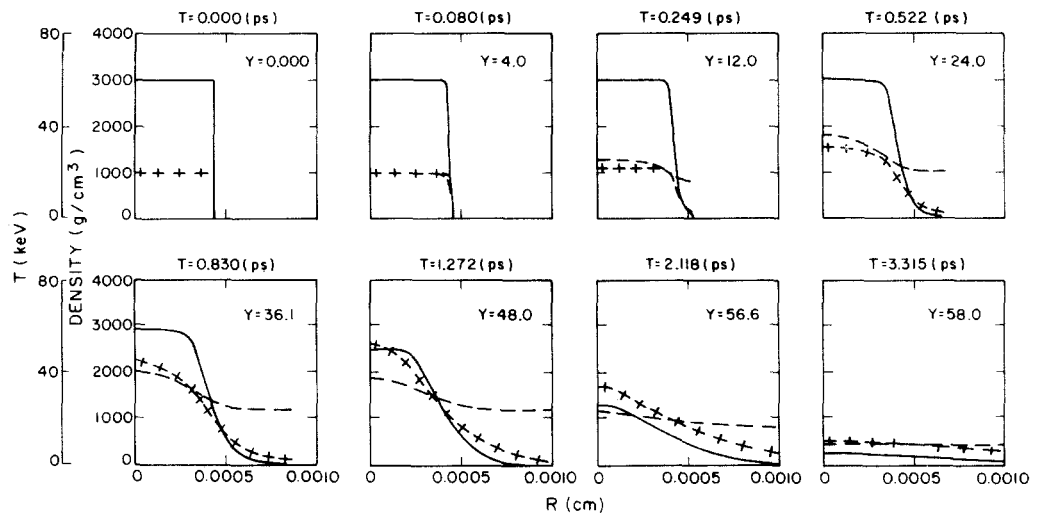FIG. 4. Burn-up and disassembly of the Fig. 2 sphere, free outer boundary.

FIG. 5. The Fig. 3 sphere with $T_i = T_e = 20$ keV initially.

For uniformly heated systems G_F becomes

$$G_0 = Y_0/m/I_0. \tag{10b}$$

At fixed ρ and m (or ρR), optimization selects a temperature that provides the best specific yield for the specific internal energy invested in the microsphere. The mass of the microsphere can then be adjusted to match mI_0 to the energy delivered to the core of the pellet in laser-pellet interaction experiments. At small ρR, where (8) applies, the optimum T is near 12 keV (borne out by our simulations), since $\langle \sigma v \rangle / C_s$ declines at larger T while I_0 rises, and since Y_0 drops as $\sim T_i^3$, dominating over the decrease in I_0 as we go to lower T. With large ρR (≥ 1.0, from the simulations), on the other hand, the optimum T declines, since bootstrap-heating can raise the microsphere to a good burn temperature, even though less I_0 is invested. In the limit, as ρR is increased, the optimum T approaches the ignition temperature, which itself is dropping from its solid density value (4 keV), as a consequence of heightened inverse bremsstrahlung.

D. Central ignition and propagating burn

A further and significant improvement in the gain factor can be made, if I is apportioned so that just a central region of the microsphere is heated to ignition temperature, under conditions that the *spherical thermonuclear burn wave* then propagates out, igniting the rest of the fuel. Such burn-wave propagation was first openly discussed in Ref. 16. Its favorable influence was implicitly included in the Ref. 1 results, however, where propagation progressively improves the yield with increasing pellet mass. Discussions of plane burn-wave propagation in solid density DT are available in the literature.[11,17,18]

Figure 6 depicts propagating burn in a 10-μg microsphere. The sphere is initially uniform at $\rho = 6 \times 10^3$ g/cm^3, so $\rho R = 4.4$. A vertical line demarks the inner 10% of the mass; it is at 20 keV; the remaining outer mass is at 1 keV. At first, the electrons bootstrap heat in the inner region, and conduct into the outer one. At the same time, the outer mass is compressed somewhat by the expanding inner fuel. The capture of α's from the center, ion conduction, and electron-ion exchange have brought $\sim$
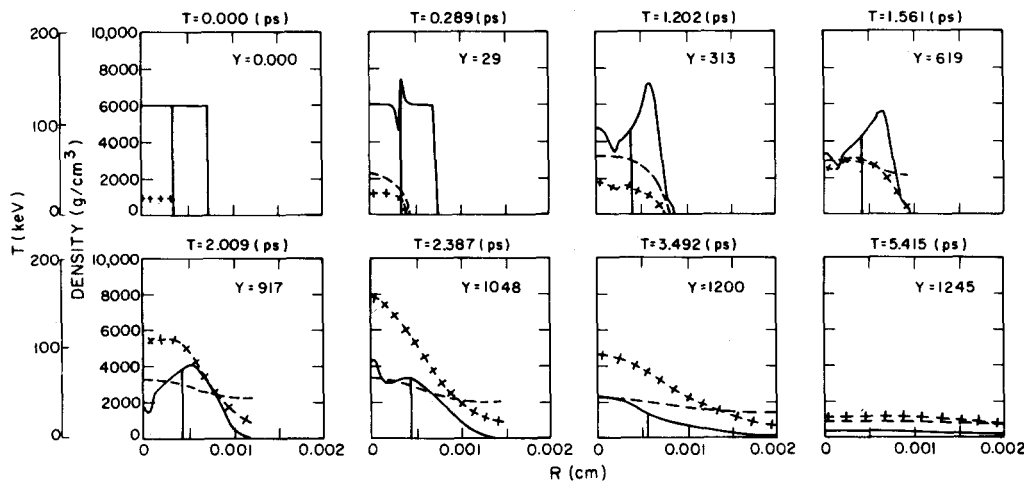
FIG. 6. Propagating burn in a 10-μg sphere; free outer boundary. Inner 10% of the mass $T = 20$ keV; remaining mass $T = 1$ keV.

40% of the outer ions to 20 keV by 1.2 psec. The outer region is then burning to high depletion. It re-implodes the center between 2 and 2.4 psec. Then finally, by 5.4 psec, the burn has been quenched by disassembly. The yield is 1.245×10^3 kJ. When this same sphere is started at a uniform, 20-keV temperature, it burns to $f_r = 0.42$, yielding 1.369×10^3 kJ. So, with central ignition we release 91% of the yield of the uniform case by investing only 18% of its energy—for a 5.2-fold multiplication in the gain-factor.

From this example we conclude that it is useful to define a multiplication factor M_c, characterizing the gain from central ignition, such that

$$G_F = G_0 M_c, \quad M_c \equiv \frac{Y}{Y_0}\frac{I_0}{I}. \quad (11)$$

then, G_0 is the gain from a uniformly heated microsphere at temperature T, internal energy I_0 and yielding Y_0 while Y is the yield from the same microsphere with a central hot spot at T, and a cooler exterior, so that a lower specific internal energy I is implied. In the Fig. 6 example, $Y/Y_0 = 0.91$, $I_0/I = 5.7$, and $M_c = 5.2$.

The multiplication from central ignition would be slightly higher, i.e., $M_c \sim 6.3$, were it not for electron degeneracy. At $\rho = 6 \times 10^3$ g/cm^3, $T_{ef} = 1.87$ keV. At 1 keV, the cold region in Fig. 6 is therefore degenerate with a specific internal energy

$$I_c = 5.8 \times 10^{-2}\left\{ T_i(\text{keV}) \right.$$

$$\left. + T_{ef}(\text{keV})\left[1 + \frac{\pi^2}{15}\left(\frac{T_e}{T_{ef}}\right)^2 + \cdots \right]\right\}(\text{kJ}/\mu\text{g}) \quad (12)$$

[following Eq. (6)] that is, 1.7 times its classical value, reducing M_c only marginally, since most of the energy still resides in the central 20 keV region.

In general, for spheres with such hot-spots, we can write

$$\frac{I_0}{I} = \frac{m I_0}{m_h I_0 + (m - m_h) I_c} = \left(f_h + (1 - f_h)\frac{I_c}{I_0} \right)^{-1}, \quad (13)$$

in which $f_h = m_h/m$ is the fraction of the pellet mass that

is hot. For effective central ignition: (a) first, the full pellet must have a large enough ρR so that, if it were uniformly hot, there would be over all α-particle recapture and bootstrap-heating, leading to a good fractional burn-up ($f_{r0} \gtrsim 0.2$) and a correspondingly high Y_0; (b) then, for an optimal M_c, the hot fraction f_h must be small —but not too small; since for $Y/Y_0 \sim 1$, the radius of the hot region must exceed λ_α for its initial burn to be sustained by bootstrap heating, while propagation ignites the neighboring cold region. These conditions imply a high density in microspheres ($\gtrsim 10^4$ solid), so degeneracy will place a significant floor on I_c/I_0. In our Fig. 6, for example, $f_h \sim I_c/I_0 \sim 0.1$.

A central hot spot is provided by the final shock collapse in optimized implosions,[1] so $M_c > 1$ can be anticipated. Also, the shock energy dumps primarily into the ions, which can increase G_F by affecting a higher early burn rate. Finally, since burn begins with the shock collapse, this moment can serve as $t = 0$ for the studies which follow.

IV. NUMERICAL RESULTS

A. Y_0

Figures 7(a)–(d) show the computed yields from uniform microspheres with various initial ρ and T.

At low densities (< 100 g/cm^3 for each of the three masses, 10, 1.0, and 0.1 μg), the $Y_0 \sim \rho^{2/3}$, in agreement with Eq. (8c). In fact, estimates from Eq. (8) are quite accurate. With 10 μg, for example, when $\rho = 10$ g/cm^3 and $T = 3$ keV, we get $\rho R = 6.2 \times 10^{-2}$ g/cm^2 and $\tau_e/\tau_r = 1.15 \times 10^{-4}$ [see Fig. 8 in which the ordinate τ_e/τ_r is simply $(\langle \sigma v \rangle / 4 C_s m_i)\rho R$ from Eq. (8a)], so $f_{r0} = 5.8 \times 10^{-5}$ by Eq.(8), and $Y = 326(10)f_r = 1.9 \times 10^{-1}$ kJ, which lies on the appropriate Fig. 7(a) curve. As density is increased, bootstrap-heating eventually raises the computed yields above the Eq. (8) predictions; this occurs for $\rho > 700$ g/cm^3 in the 10-μg pellet. Finally, with still further increases in ρ, the yield curves flatten out from fuel depletion. As we go from 10 to 0.1 μg, the densities characterizing the onset of depletion are 10^3, 3×10^3, and 10^4, corresponding to the yields 600, 60, and 6 kJ, respectively.

We considered that the prediction of ignition for high-

FIG. 7. Y_0 vs ρ in spheres of: (a) 10 μg, (b) 1 μg, and (c) 0.1 μg. The dashed curves in (a) are for just the inner 10% of the mass at 10 and 20 keV. The x data were recalculated with an independent nonequilibrium code. The + data include neutron energy redeposition for $T = 3$ keV. (d) Details of the temperature dependence in the 10 μg sphere.
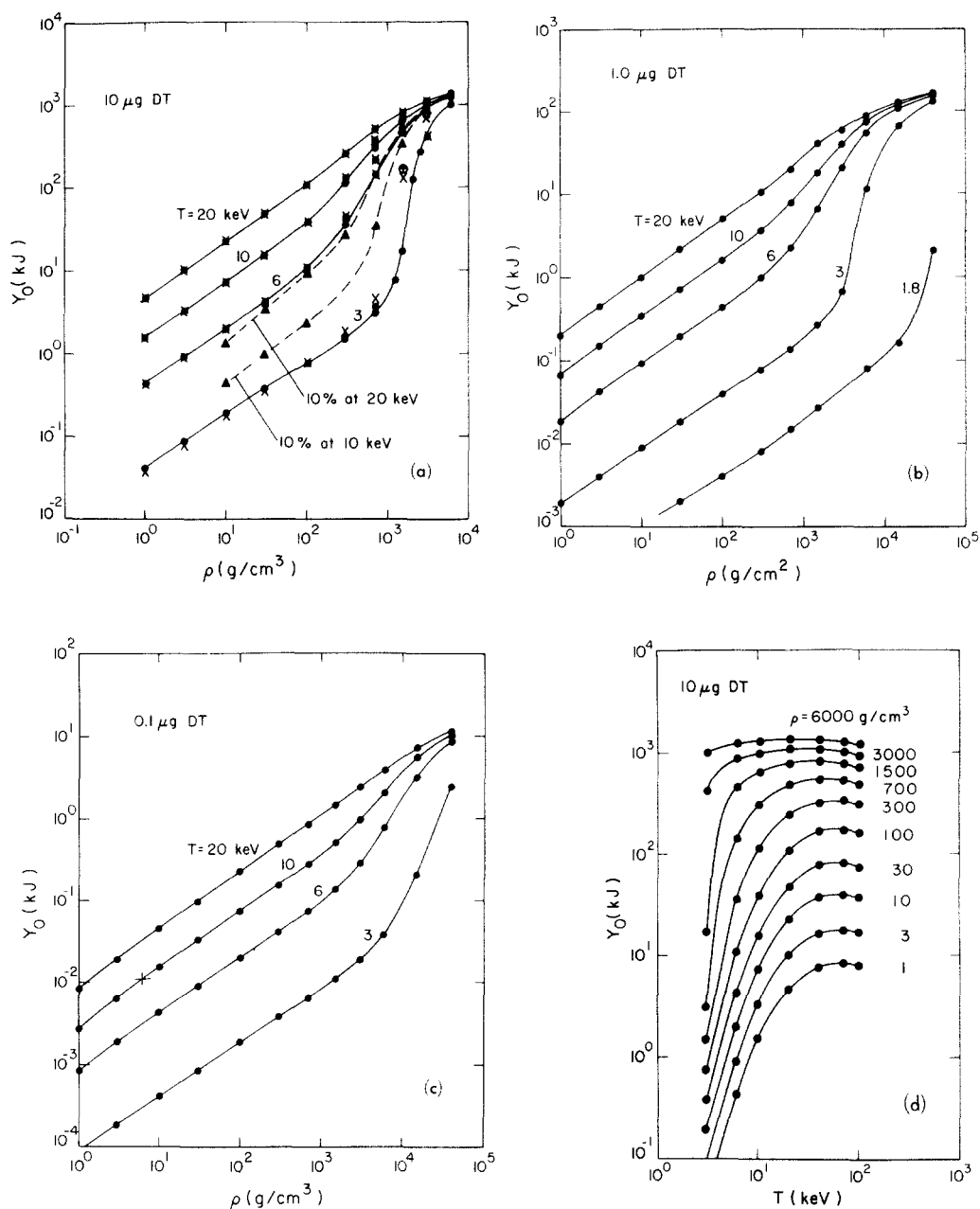
density DT at the 3 keV of our code might sensitively depend on its use of a radiation diffusion treatment. Consequently, our 10-μg results were checked by a separate series of calculations with an independent, nonequilibrium code that does frequency dependent Monte Carlo radiation transport (and also Monte Carlo α-particle transport). Its results are the x-sign data in Fig. 7(a). Generally, the two sets of results are in good agreement. However, the Monte Carlo calculations show no descent below a $Y_0 \sim \rho^{2/3}$ dependence in the $100 < \rho < 700$ g/cm^3 range like the dip predicted by the diffusion treatment. Also, the x-data bootstrap at slightly lower ρ.

Figure 7(d) more clearly shows the T dependence of Y_0 in 10 μg spheres. The peak yields are near 40 keV. But, the dependence becomes increasingly flatter as we go to higher density, so that at 3000 g/cm^3, Y_0 is nearly constant between 10 and 70 keV.

In Fig. 7(a), we have included the yields obtained when

only the inner 10% of the 10-μg pellet is at 10 and 20 keV, while its outer mass starts at 1 keV. Clearly, these yields have the same general ρ dependence (including net bootstrapping above 700 g/cm^3) as the curves for uniformly heated microspheres. At 100 g/cm^3, λ_α is too large for either bootstrapping or effective propagation. Consistently, from the Fig. 7(a) data with Eqs. (11) and (13) (and accounting for degeneracy in the cold region), we calculate $M_c = 0.23$ and 0.47 with the hot spot at 10 and 20 keV, respectively. At 10^4 g/cm^3, on the other hand, the yields are essentially the same as with uniform heating, so $M_c \rightarrow I_0/I \sim 3.9$, and 5.7 for the two temperatures. Still it should be recognized that even at densities where propagation fails, it is advantageous to apportion the internal energy in a central hot spot, since this can increase the yield by establishing a higher average burn rate. With the 10 keV hot spots, for example, the average pellet temperature is 2.5 keV, but the yields roughly equal those from 4-keV pellets until $\rho < 1000$ g/cm^3, when the
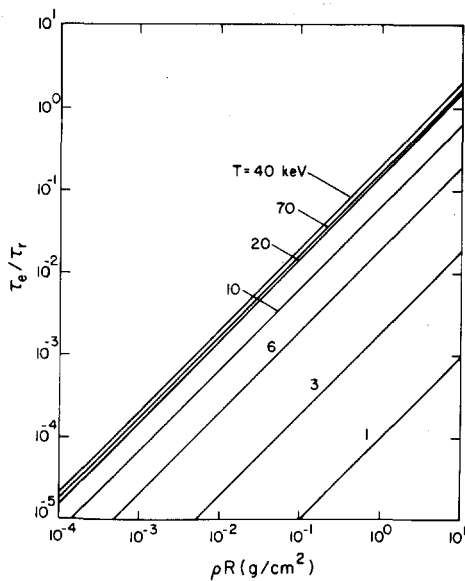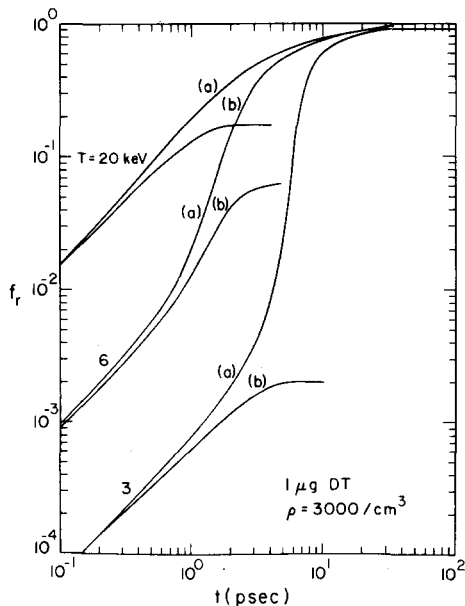
FIG. 8. τ_e/τ_r vs ρR.

FIG. 9. Time dependence of the burn fraction $f_r(t)$ in 3, 10, and 20 keV, 1 μg sphere with (a) fixed, and, (b) free outer boundaries.

situation further improves because propagation becomes significant.

B. $f_r(t)$

Figure 9 shows the time dependence of the burn-up fraction $f_r(t)$ in 1-μg pellets at 3000 g/cm³. The results are for both a fixed and free outer boundary; they include the Fig. 2, 4 and 5 runs. The temperatures are 3, 6 and 20 keV for which the reaction times $\tau_r(T_i) = 710$, 51 and 3.3 psec, respectively.

With a fixed boundary and $T = 3$ (compare Fig. 2), $f_r(t)$ undergoes linear growth to 0.5 psec and then bootstrap heating thereafter. The heating is strongest ($f_r \sim t^{7.5}$) from 4 to 6 psec. Depletion slows the burn rate for $f_r > 0.3$. The $T = 6$ result is similar, but with the strong bootstrapping coming in sooner—from 1 to 3 psec. With

$T = 20$, there is nearly linear burn to 2 psec followed by depletion.

With the free boundary, 90% of Y_0 is out in each of the three cases by $t = R/2C_s$ [$R/C_s(T_i) = 6.9$, 4.8, and 2.7 psec]. Thus, we see that the effective burn time is not $\tau_e = R/4C_s$ [Eq. (8)], as at lower densities, since all three cases are bootstrapping. At $T = 3$ keV, the unbootstrapped final $f_r \equiv f_{r0}$ [extrapolating the Fig. 7(b) curve] would be 1.1×10^{-3}, while the observed f_{r0} is 2×10^{-3}. The $T = 6$ case disassembles, while still in the strong bootstrap phase. In fact, its effective burn time (based on $T \equiv 6$ keV) exceeds R/C_s. Depletion is unimportant in these three cases since they disassemble leaving $f_{r0} < 0.2$.

C. f_{r0} and G_0 vs ρR

When Y_0 is converted to f_{r0} and the Fig. 7(a)–(c) data are plotted vs ρR, it collapses to one curve for each of the temperatures studied with the mass dependence explicitly removed—except for $\rho R \gtrsim 2.0$, where degeneracy effects noticeably reduce f_{r0} at small m and T [see Fig. 10(a)].

From Eq. (8), this scaling was anticipated for $\rho R < 0.2$ g/cm², for which there is little bootstrap heating. But, it also works for larger ρR, because λ_α/R [Eq. (3e)] also scales with ρR. Equation (3e) indicates that at 10 keV and $10^3 \leq \rho \leq 10^4$ g/cm³, for example, α's from the center of the microsphere have $\lambda_\alpha < R$ for $\rho R \gtrsim 0.73$. Clearly, the degree of bootstrap heating depends on the fraction of α's f_α recaptured in the pellet. In Fig. 10(b), we plot the f_α's calculated in our various runs. Good scaling with ρR is evident, but the larger masses recapture α's somewhat more effectively (2–6%) at all ρR.

This is consistent with a greater energy absorption rate from an increase in the log terms in Eq. (3b), as we go to the smaller ρ corresponding to larger m at fixed ρR. With different masses $m = 4\pi\rho R^3/3$ this correspondence is, of course,

$$\rho \sim (\rho R)^{3/2}/m^{1/2} \sim \text{const } m^{-1/2}. \quad (14)$$

By now it should be evident that it is extremely difficult to burn more than 30% of the fuel. Above $f_r = 0.3$ depletion begins to severely reduce the effective burn rate, requiring increasingly longer inertial confinement times. At 20 keV and $\rho R \geq 1.28$, the effective burn time is $\tau_b = R/2.4C_s$ (see Fig. 6), due to the bootstrap heating. The use of $t = \tau_b$ in Eq. (2) and the conversion $\tau_b/\tau_r = 1.7(\tau_e/\tau_r) \sim 0.32\rho R$ (on the average between 20 and 70 keV—see Fig. 8) gives

$$f_{r0} \simeq \frac{\rho R}{6.3 + \rho R}, \quad \begin{array}{l} \rho R \gtrsim 1 \\ 20 < T < 70 \text{ keV}, \end{array} \quad (15)$$

which predicts $f_{r0} \simeq 0.41$ at $\rho R = 4.4$, for example, in agreement with the Fig. 10(a) results.

We must remember, however, that the 14 meV neutrons have a 22-cm mean free path[19] in solid density DT. In analogy, therefore, with Eq. (3e),

$$\lambda_n/R = 4.6/\rho R. \quad (16)$$

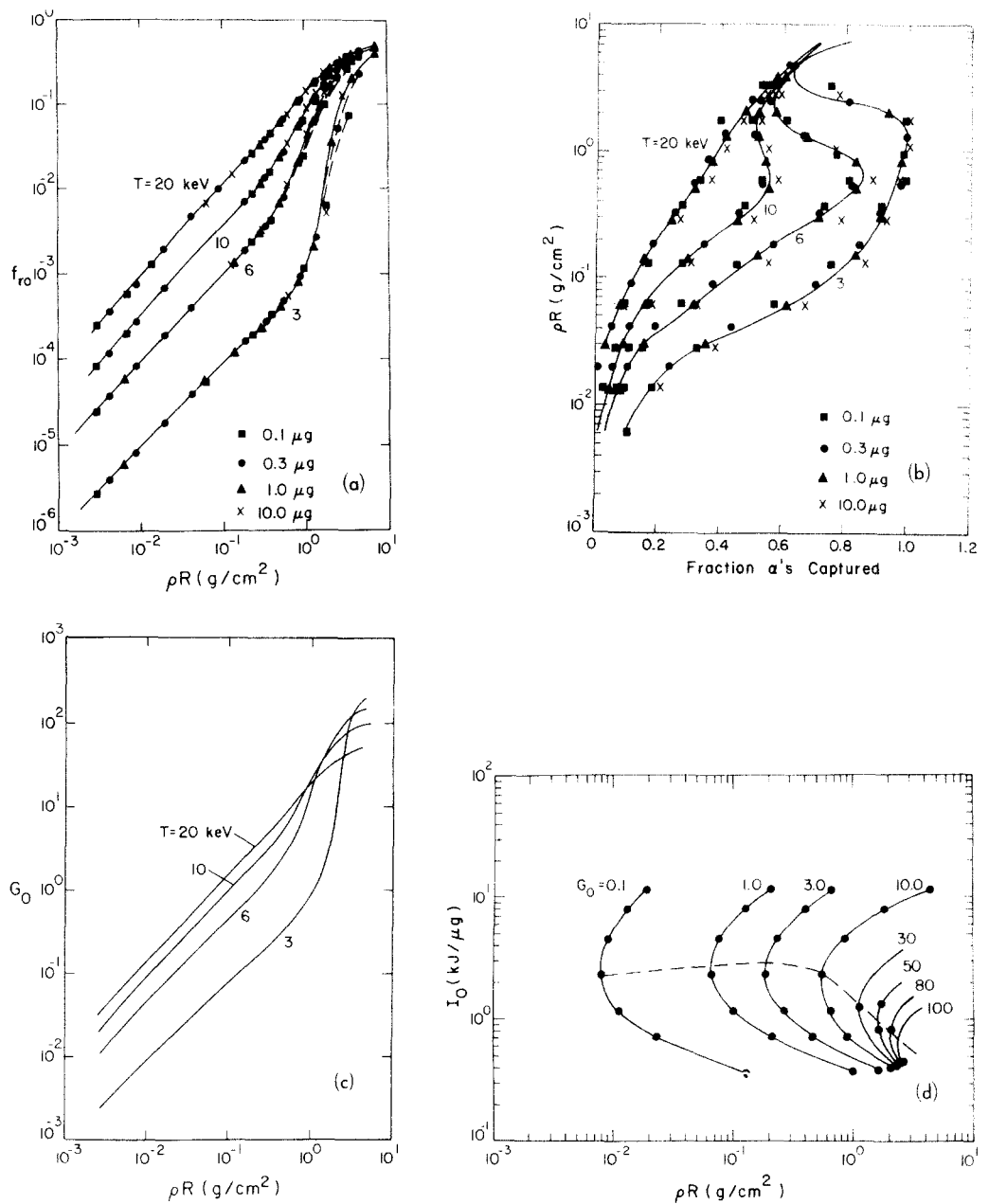So for $\rho R \gtrsim 4.6$ and $f_{r0} \gtrsim 0.42$, neutron energy is recap-

FIG. 10. ρR dependence of (a) the burn-up fraction f_{ro}, (b) the fraction of α's recaptured f_{α}, and (c) the gain-factor G_0 for uniformly heated spheres, (d) isogain factor contours vs I_0 and ρR.

tured, complicating the phenomenology. Neutron recapture effects are discussed in Sec. IV.

The gain factor G_0 also scales well with ρR. The Fig. 10(c) curve is a composite constructed from an overlay of all our run results. It applies for $\rho < 6000$ g/cm³. Above this density, degeneracy effects begin to seriously split each T curve, giving lower gains as m decreases. We see that G_0 exceeds unity at 20 keV for $\rho R > 0.1$. For $\rho R \sim 1$, the T curves cross, and the bootstrap-heating permits us to achieve higher gain factors by starting at lower initial temperatures. Figure 10(d) is derived from 10(c) and gives the isogain factor contours for uniformly heated microspheres with $\rho < 6000$ g/cm³. It shows that for each ρR there is an optimal I_0 giving the best G_0. At $\rho R = 2.15$ ($10^4 \times$ solid density with 10 μg), the best $G_0(\gtrsim 80)$ comes for $I_0 = 0.8$ kJ/μg. The dashed line through the minimal I_0 values give the phenomenological rules: $I_{0|min} \sim (\rho R)^{-0.8}$, $G_{0|max} \sim (\rho R)^{1.58}$, $0.56 \lesssim \rho \lesssim 2.45$. Note that if the effects of depletion can be circumvented, so that all the fuel is burned, then starting it at the

classical ignition temperature,[9] $T_i = T_e = 4$ keV, gives a theoretical maximum $G_0 = 699$.

D. M_c

To get a quantitative understanding of the possible advantages from central ignition, we conducted a series of runs for microspheres of different ρR and m, in which an inner fraction of the mass f_h was started hot at 10 keV, while the remaining fraction was set at 1 keV (as for Fig. 6). When $f_h = 1$, it follows that $Y = Y_0$, $M_c = 1$ [see Eq. (11)] and $G_F = G_0$. In each series of runs, f_h was decreased until $M_c \ll 1$.

Figure 11(a) shows that for $\rho R \gtrsim 2$, the ratio Y/Y_0 declines gradually until f_h reaches some threshold value, after which Y drops away extremely rapidly. From the intersections of asymptotes drawn tangent to the flat portions of the 10-μg curves, we have determined that at the drop-off $f_h = f_{h|min} = 0.1$, 0.015, and 0.002 for $\rho R = 1.35$, 2.15, and 3.90, respectively. Since $f_h = m_h/m = (\rho R_h)^3/(\rho R)^3$, these results imply $f_{h|min} = (0.5)/(\rho R)^3$
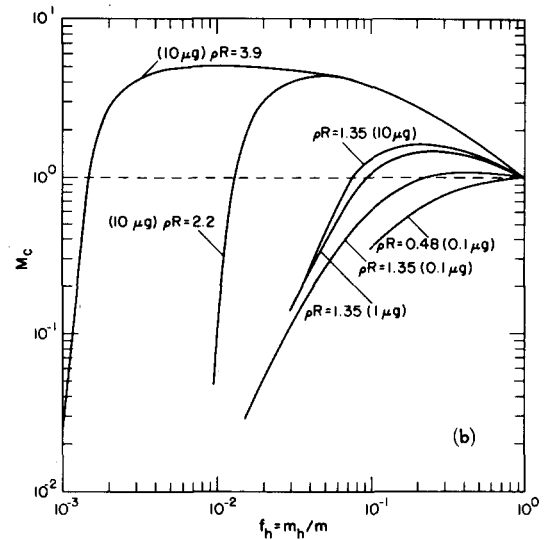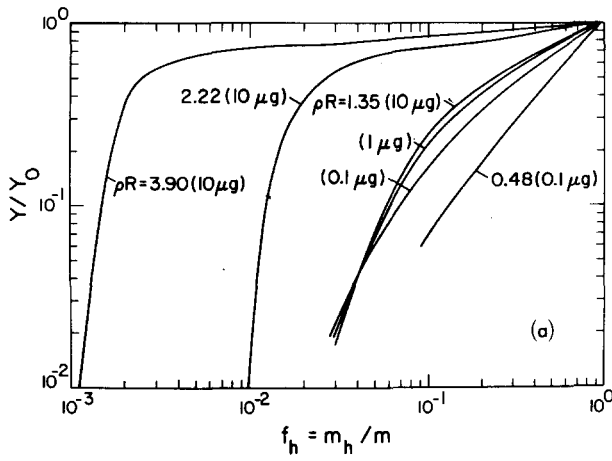
FIG. 11. Dependence on the fraction of mass hot f_h with central ignition of (a) the scaled yield Y/Y_0, and (b) the central ignition multiplier M_c.

and thus $\rho R_{h|min} = 0.8$. But with this ρR_h (at 16 keV and with $10^3 \le \rho \le 10^4$ g/cm^3) $\lambda_\alpha/R_h \simeq 1$. Assuming, then, that bootstrap heating provides a 16 keV environment, on the average, we conclude that λ_α serves as a minimum radius for hot spots inaugurating successful propagation. Clearly, propagation must fail in the $\rho R = 0.48$ (0.1 μ g) spheres, since for them $f_{h|min} = 0.5/(0.48)^3 \simeq 4.0$, i.e., $\lambda_\alpha \gg R$. The gradual decline in Y/Y_0 for $f_{h|min} \ll f_h \lesssim 1$ derives from the additional time, relative to the uniform case, required for propagated ignition of the fuel.

Since, generally, $Y/Y_0 < 1$ with central ignition, gain multiplication must come from a reduction in the required internal energy. From Eq. (13), the maximum $I_0/I \to I_0/I_c$, $f_h \ll 1$. At $\rho = 2130$ g/cm^3, for example, $I_0/I_c = 9.5$ (it is not 10 because of degeneracy—see the equation of state data in Fig. 12). The multiplications M_c computed for various f_h are plotted in Fig. 11(b). The competing effects of decreased I, and decreased Y give a maximum $M_c^* = 4.1$ at $\rho R = 2.2$ in the 10-μ g pellet. The unfavorable influence of degeneracy is evident in the $\rho R = 1.35$ results which show M_c^* dropping from 1.5 to 1.05, as m changes from 10 to 0.1 μg. From the M peaks in Fig. 11(b), we have determined the phenomenological rule, $m^*(g) = 4.9 \times 10^{-2}\rho^{-3/2}$, for the optimal pellet mass at each density examined. With it, we conclude that the best choice for f_h is

$$f_h^* = \frac{3(4.9 \times 10^{-2})\rho^{-3/2}}{4\pi\rho R^3} = 1.2 \times 10^{-2}\rho^{1/2}/(\rho R)^3. \quad (17)$$

For example, $f_h^* \simeq 0.05 \simeq 3f_{h|min}$ for $\rho = 2130$ g/cm^3 and $\rho R = 2.2$ in the 10-μg pellet.

V. FINAL CONSIDERATIONS

In laboratory laser-pellet interaction experiments, the yield ratio $Y_R = Y/E_L$ is of consequence; E_L is the energy absorbed from the laser. Also of importance is the coupling efficiency $\varepsilon = mI/E_L$ between the absorbed E_L and the internal energy mI of the microsphere core of the pellet;

$$Y_R \equiv Y/E_L = \frac{\varepsilon Y}{mI} = \varepsilon G_F = \varepsilon G_0 M_c. \quad (18)$$
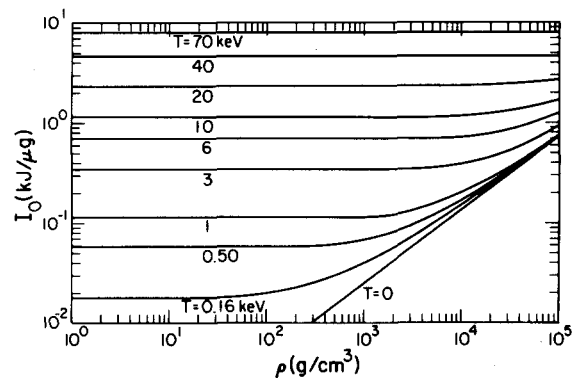

FIG. 12. I_0 vs ρ in equimolar DT for $T_e = T_i = T$, $T_r = 0$; note the asymptotic approach to the degeneracy floor on I_0 for $T < 10$ and $\rho \to 10^5$g/cm^3.

In this paper, we have examined the dependence of G_0 and M_c on various possible initial states of the fuel. A general connection between Y_R and E_L cannot be drawn, however, in the absence of more precise information on the core conditions established by the laser-driven hydrodynamics, as implicitly determined in the Ref. 1 calculations.

Still, to relate the present work to our earlier results for laser-imploded pellets, we give the following example: Let $\varepsilon = 0.1$. Suppose the laser compresses the 10-μg core of a larger pellet to $10^4 \times$ solid density, so its $\rho R = 2.2$. Imagine that a final shock collapse leaves the optimal mass fraction at 10 keV and the background at 1 keV. Then $f_h^* = 0.05$ and $M_c^* = 4.1$ [Fig. 11(b)]. The uniform gain-factor $G_0 = 62$ at 10 keV and this ρR [Fig. 10(c)]. So Eq. (17) predicts $Y_R = 0.1(62)4.1 = 25.4$. At 10 keV, $I_0 = 1.22$ kJ/μg, while $I_0/I = 6.0$, when $f_h = f_h^*$. This means that 0.20 kJ/μg is needed, for a total of 2 kJ over the whole 10-μg microsphere. In accordance with the value of ε, it follows that $E_L = 20$ kJ. This yield ratio and input energy agree with the Ref. 1, Fig. 2(e) optimized results for shells. The yield is $Y = Y_R \times E_L = 508$ kJ. It represents the burn-up of 10 μg to $f_{r0} = 0.16$. At 10 keV, Fig. 10(a) predicts $f_{r0} \simeq 0.22$; multiplication by the correction $Y/Y_0 = 0.7$ [Fig. 11(a)] for central ignition also

gives $f_{r0} = 0.16$. Finally, to complete the picture, we recall that Ref. 1 recommended $E_L = 0.7$ kJ/μg, based on the full pellet mass M for optimized yields. This sets M at 28.6 μg. So, in fact, the microsphere core is roughly 35% of the mass.

A few additional comments should be made about our high density results. (a) First, recall that the neutron mean free path, Eq. (15), falls within the microspheres, $\lambda_n < R$, for $\rho R \lesssim 4.6$. Therefore, at $\rho R = 2.2$, for example, some fractional recapture of the neutrons occurs, and, on the average, 4 meV is transferred to the DT per interaction (reduced from 14 meV by the mass differential). Consequently, we made a small subgroup of runs, including S_n neutron transport. These have shown, for example, that neutron recapture lowers the density threshold for 3-keV ignition in the 10-μg microsphere, giving 100 kJ yields at only $\rho = 1000$ g/cm^3 [the $\oplus$ data point in Fig. 7(a)]—instead of at 1500 g/cm^3, as computed with α-recapture alone. (b) Then, note the following disclaimer to our results involving degeneracy at high density. Although the thermodynamics has been corrected for degeneracy, e.g., the internal energy in the 1- keV outer regions of the pellets of our propagation study [Sec. III D], we use classical transport coefficients and classical mean free paths to determine the energy flow. The inclusion of degeneracy in the electron thermal conductivity and in the cross section for α particles against degenerate electrons, as examples, could significantly modify the efficiency of central ignition.

Early laser-initiated DT burn experiments will most readily involve unignited burn—the $Y_0 \sim \rho^{2/3}$ regime. The practical achievement of extreme DT densities serves as a special challenge. The neutrons produced experimentally are a useful diagnostic; 3.6×10^{14} are created per kilojoule of thermonuclear energy yield, or roughly 10^{17} neutrons are available from the complete consumption of 1 μg of DT. Figure 13 shows the isoneutron contours, derived principally from the Fig. 10(a) burn-up data for disassembling spheres. It gives the neutrons produced per microgram of DT versus the specific internal energy of the fuel and its ρR. The ρR of 1 μg of DT at solid density is 2.2×10^{-3}. From Fig. 13 we conclude that with 1 kJ uniformly deposited in the 1 μg, $\sim 6 \times 10^{12}$ *neutrons can be released at solid density*. The important point to be made here is that, although such a neutron release is impressive by conventional Controlled Thermonuclear Reaction standards, it is in no way proof of large compressions, and represents an output energy that is 60-fold short of breakeven.

We see that as experiments begin with the new 1 to 10-kJ laser systems, the production of 10^{13} neutrons/kJ of laser input can serve as a bench mark, implying effective absorption, and presumably, some compression, compensating for the laser energy lost to blow-off. Progress toward a breakeven demonstration can then be measured by how close we come to the production of 10^{15} neutrons/kJ, as the technology advances.

ACKNOWLEDGMENTS
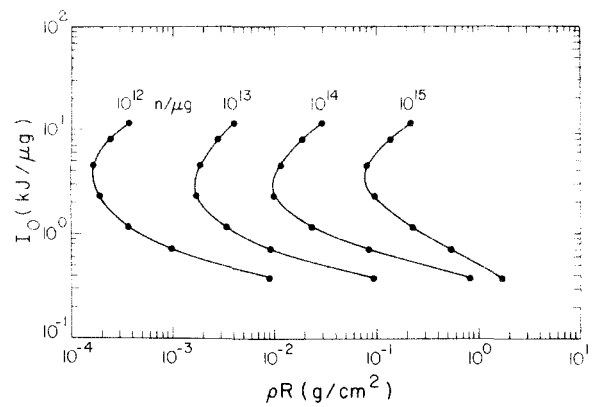
FIG. 13. Isoneutron output contours vs I_0 and ρR.

APPENDIX A

The use of solid DT pellets in laser-interaction experiments presents certain technical difficulties, principally in the area of cryogenics. These may be avoided, at least in early investigations, by the use of LiDT targets. To examine the ramifications of this possibility, the thermonuclear-burn characteristics of LiDT spheres have been calculated. Figures 14(a)–(c) give our results for the burn-up fraction f_{r0}, gain G_0, and gain multiplication M_e of Li^6 DT microspheres of mass $m = 10$ μg.

This compound has a mean atomic number $\bar{Z} = 2$, $\bar{Z^2} = 5$, and a mean atomic mass number $\bar{A} = 4.25$—compared to $\bar{Z} = 1$ and $\bar{A} = 2.5$ for pure DT. In LiDT, the number fraction of deuterons is $f_D = 0.5$—one deuteron for every two LiDT's; in pure DT, $f_D = 1.0$. The thermonuclear yield from the complete burn-up of this fuel, i.e., $f_{r0} \to 1$, by the D–T reaction is 95.9 kJ/μg.

By arguments similar to those accompanying Eq. (8a), we find that for Li^{6}DT spheres,

$$f_{r0}|_{LiDT} = f_D \left(\frac{\bar{A}_{DT}}{\bar{A}_{Li^6DT}} \right)^{1/2} f_{r0}|_{DT} = 0.383 \, f_{r0}|_{DT}, \quad (A1)$$

in the absence of significant bremsstrahlung loss, bootstrap heating, and fuel depletion. The Li^{7}DT isotope gives ~ 5 % less burn-up, since its $\bar{A} = 4.75$. Figure 14(a) results agree with this, Eq. (A1), behavior in the $\rho R < 3 \times 10^{-2}$ regime with $T = 3$, and for $\rho R < 8 \times 10^{-2}$ for $T \geq 6$.

The rate of bremsstrahlung loss per unit mass in each fuel has the dependence $\partial I/\partial t|_b \sim (\bar{Z^2}/\bar{A^2})(ZT_e^{1/2})$, while the rate of thermonuclear energy generation from the D–T reactions obeys $\partial I/\partial t|_t \sim (f_D/\bar{A})^2 \langle \overline{\sigma v} \rangle$. The specific bremsstrahlung rate is 3.46 times higher in LiDT; the specific energy production rate is 11.6 times lower. In the range $T = 3$ to 10 keV, $\langle \overline{\sigma v} \rangle \sim T^{3.5}$, so to compensate for the increased loss from bremsstrahlung, T must be
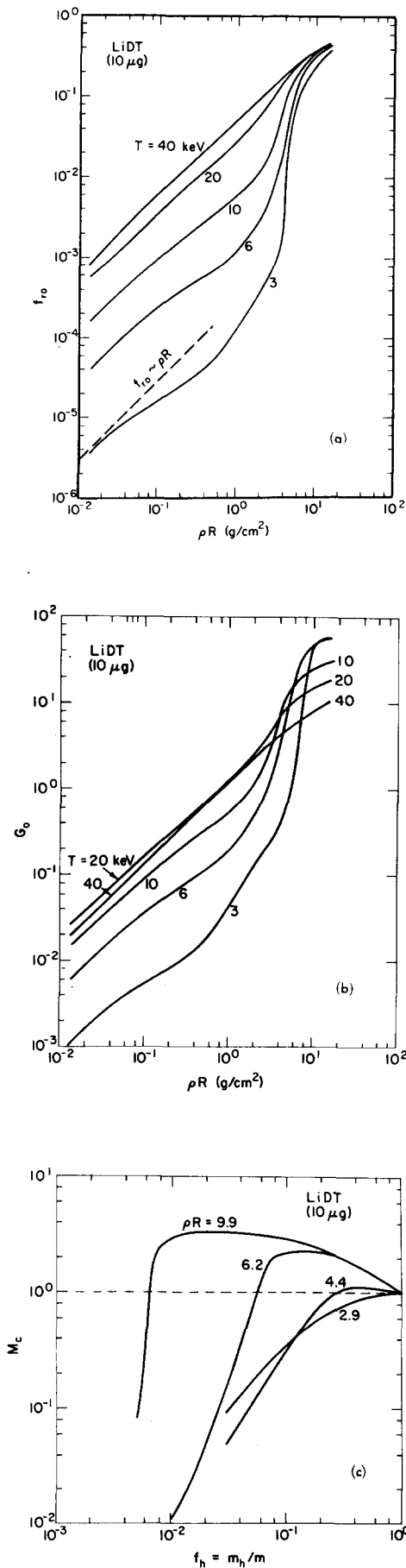
FIG. 14. (a) ρR dependence in Li^{6}DT of (a) the fractional burn-up f_{r0}, (b) the gain factor G_0, and, (c) the multiplication from central ignition with different mass fractions f_h at 10 keV.

increased by a factor of 3.4. Thus, while the ignition temperature is 4 keV in DT, in LiDT it rises to 13.7 keV. This value applies assuming $T_e = T_i$ equilibrium, negligible inverse bremsstrahlung, and redeposition of the 3.5-meV α-particle reaction products alone. With complete neutron energy redeposition as well, i.e., a total of 17 meV redeposited per reaction, the LiDT ignition temperature drops to 8.1 keV. Finally, with increased inverse bremsstrahlung at large $\rho^2 R$, giving a short photon mean free path [as in Eq. (5)], the ignition temperature falls below 3 keV, as evident from the $f_{r0}|_{\text{LiDT}} = 0.3$ calculated for $\rho R = 15$ and $T = 3$ keV. At this temperature, one sees increased f_{r0} from α redeposition for $0.5 \lesssim \rho R \lesssim 2.2$, and a further, more pronounced, increase from the neutron energy redeposition for $\rho R > 2.2$. The total scattering cross-section for 14-meV neutrons[19] is ~ 0.9 b off DT, and ~ 1.5 b off Li^6. This gives a neutron mean free path of 3.5 cm in solid density Li^6 DT, so that in comparison to the radius R of a microsphere

$$\left.\frac{\lambda_n}{R}\right|_{\text{LiDT}} = \frac{3.0}{\rho R}. \tag{A2}$$

This is consistent with the strong f_{r0} rise for $\rho R > 2.2$. The cross sections increase with lower neutron energies. Thus, following the first scatter, subsequent events become more probable, aiding the energy redeposition. The three temperature code was used in all the LiDT simulations; its S_n neutronics treatment accounts for the total energy deposition from these multiple scatterings. Additional energy (and tritium) can be generated by the reaction

$$n + \text{Li}^6 \rightarrow \alpha + T + 4.17 \text{ MeV}.$$
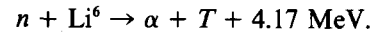
At 14 meV, however, the cross section for this reaction is only 0.026 b (~ 93 times lower than the net scattering cross section), so the yield it adds is small. Still, the effects of this reaction are included in the Fig. 14 results.

For large ρR and $T = 20 - 40$ keV

$$\left.f_{r0}\right|_{\text{LiDT}} \sim \frac{\rho R}{18.3 + \rho R} = 0.45 \qquad \text{when } \rho R = 15. \tag{A3}$$

This can be compared with the Eq. (15) result for DT. Again, roughly a three-fold increase in ρR is needed before the LiDT burn-up fraction approaches that of DT.

The specific internal energy of fully ionized Li^{6}DT, taken as a perfect gas, is

$$\left.I\right|_{\text{LiDT}} = \frac{3}{2}\frac{k(T_i + \overline{Z}T_e)}{\overline{A}m_A} \tag{A4}$$

$$= 3.41 \times 10^{-2}[T_i(\text{keV}) + 2T_e(\text{keV})] \text{ kJ}/\mu\text{g},$$

where m_A is the atomic mass unit 1.66×10^{-24} g. This is 88% of the specific internal energy of pure DT for $T_e = T_i$ [see Eq. (9)]. The specific yield from our uniform LiDT spheres is $Y_0/m = 95.9 f_{r0}|_{\text{LiDT}} \text{kJ}/\mu\text{g}$. Burn performance is measured by the gain factor

$$\left.G_0\right|_{\text{LiDT}} \equiv \frac{Y_0}{mI_0} = \frac{95.9 f_{r0}|_{\text{LiDT}}}{I_0(\text{kJ}/\mu\text{g})}. \tag{A5}$$

Figure 14(b) shows that the gain at 6 keV exceeds the 20-keV gain for $\rho R \gtrsim 5.0$; in DT, this crossover occurs for $\rho R \approx 1$. Depletion limits the 6-keV LiDT gain to $G_0(\rho R > 15) \to 58$; the corresponding limit in DT is $G_0(\rho R > 4) \to 180$.

Figure 14(c) gives the results of the Sec. III D M_c calculation for LiDT. An inner fraction f_h of the initial pellet mass was started at 10 keV; the remaining outer mass was at 1 keV. We see that at $\rho R=6.2$, for example, central ignition provides an $M_c \simeq 2$ [see Eq. (11)] with only $\sim 6\%$ of mass heated to 10 keV. The comparable DT figure is $M_c(\rho R \simeq 2.2) = 4$.

The optimally imploded DT spheres of Ref. 1 achieved a peak ρR near 1.9. Our most recent, refined calculation with the Ref. 1 code employing nonlocal α energy deposition predicts a $Y_R \simeq 25$ [see Eq. (18)] from a 7.5-μg sphere, absorbing 5.3 kJ of 10.6-μ laser light. Moreover, these calculations predict that an LiDT sphere of the same mass will compress to $\rho R=6.3$, giving a peak $Y_R = 1.5$, under the same time-tailored pulse, run until 26 kJ has been deposited in the pellet.

Under adiabatic compression, $I_0 \sim \rho^{2/3} \sim \rho R$. The input energy required for central ignition should, in general, vary as $E_{IN} \sim I_0/M_c$. Thus, we may anticipate that

$$E_{IN|_{LiDT}} \Big/ E_{IN|_{DT}} = \left(\frac{\rho R}{M_c}\right)_{LiDT} \Big/ \left(\frac{\rho R}{M_c}\right)_{DT}$$

$$= \left(\frac{6.3}{2}\right) \Big/ \left(\frac{1.9}{4}\right) \simeq 6 \qquad (A6)$$

is required in optimal implosions, as we have calculated. Finally, since under comparable conditions, the gain factors $G_{0|_{DT}}/G_{0|_{LiDT}} = 2.7$, we see that the calculated seventeen-fold reduction in Y_R for optimally imploded LiDT spheres is consistent with our Fig. 14 results.

APPENDIX B

I. Three temperature code

Our one-dimensional, three-temperature, Lagrangian code has, in spherical geometry, the equations of motion

$$\frac{\partial u}{\partial t} = -\frac{1}{\rho}\frac{\partial}{\partial r}(P + q) = -r^2\frac{\partial}{\partial m}(P + q), \qquad (B1)$$

in which $m = \int_0^r \rho r^2 dr$ is the mass/st, $\rho = 1/v$ with v the specific volume, and $\partial r/\partial t = u$. P is the sum of the three-fluid pressures, i.e., $P \equiv P_e + P_i + P_r$, and q is the Von-Neuman artificial viscosity.

The coupled energy equations are

$$\frac{\partial T_i}{\partial t} = \frac{1}{C_{vi}}\left[\dot{S}_i - \left(P_i + q + \frac{\partial I_i}{\partial v}\right)\frac{\partial v}{\partial t} - A_{ie}(T_i - T_e)\right.$$

$$\left. + \frac{v}{r^2}\frac{\partial}{\partial r}\left(r^2 K_i\frac{\partial T_i}{\partial r}\right)\right], \qquad (B2a)$$

$$\frac{\partial T_e}{\partial t} = \frac{1}{C_{ve}}\left[\dot{S}_e - \left(P_e + \frac{\partial I_e}{\partial v}\right)\frac{\partial v}{\partial t} - A_{er}(T_e - T_r)\right.$$

$$\left. + A_{ie}(T_i - T_e) + \frac{v}{r^2}\frac{\partial}{\partial r}\left(r^2 K_e\frac{\partial T_e}{\partial r}\right)\right], \qquad (B2b)$$

$$\frac{\partial T_r}{\partial t} = \frac{1}{C_{vr}}\left[-\left(P_r + \frac{\partial I_r}{\partial v}\right)\frac{\partial v}{\partial t} + A_{er}(T_e - T_r)\right.$$

$$\left. + \frac{v}{r^2}\frac{\partial}{\partial r}\left(r^2 K_r\frac{\partial T_r}{\partial r}\right)\right]. \qquad (B2c)$$

Each equation is derived using the chain rule

$$\frac{\partial I}{\partial t} = C_v\frac{\partial T}{\partial t} + \frac{\partial I}{\partial v}\frac{\partial v}{\partial t},$$

where

$$C_v \equiv \frac{\partial I}{\partial T}.$$

If the ions and electrons were perfect gases, then relations

$$P_i = 2/3\,\rho I_i, \quad I_i = 3/2\,kT_i/m_i, \quad C_{vi} = 3/2\,k/m_i,$$
$$P_e = 2/3\,\rho I_e, \quad I_e = 3/2\,ZkT_e/m_i, \quad C_{ve} = 3/2\,Zk/m_i, \qquad (B3)$$

would apply. In fact, there is a vast spectrum of real material effects, including: phase changes, dissociation, ionization, pressure ionization, and degeneracy, which alter the Eqs. (B3), so that for our calculations their equivalents are obtained from carefully compiled equations-of-state tables, as are the derivatives $\partial I_{i,e}/\partial v$.

The radiation diffusion treatment was included to examine changes in ignition temperature from the increased opacities at high density. The use of Eq. (B2c) assumes that the photons achieve Planckian equilibrium, characterized by a radiation temperature T_r at a rate much faster than their equilibration rate with local electrons, or the rates characterizing the changes of other significant parameters in each burn sequence. The radiation is, thus, characterized by a pressure, specific internal energy, and specific heat,

$$P_r = \frac{I_r\rho}{3}, \quad I_r = \frac{4\sigma}{c\rho}T_r^4, \quad C_{vr} = \frac{4I_r}{T_r}.$$

The fields are coupled by the coefficients $A_{ie} = C_{ve}\nu_{eq}$:

$$\nu_{eq} = \frac{8(2\pi)^{1/2}m_e^{1/2}e^4N_A^2}{3}\left(\frac{Z^2}{A^2}\right)\ln\Lambda_{ei}\frac{\rho}{(kT_e)^{3/2}}\left[1 - \frac{3}{2}\frac{T_i}{T_e}\frac{m_e}{m_i}\right], \qquad (B4a)$$

$$K_i = 20\left(\frac{2}{\pi}\right)^{3/2}\frac{(kT_i)^{5/2}k}{m_i^{1/2}e^4Z^4\ln\Lambda_i}, \qquad (B4b)$$

$$K_e = 20\left(\frac{2}{\pi}\right)^{3/2}\frac{(kT_e)^{5/2}k\varepsilon\delta_T}{m_e^{1/2}e^4Z\ln\Lambda_{ei}}, \qquad (B4c)$$

from Spitzer,[7] in which

$$\varepsilon\delta_T = \frac{0.43Z}{(3.44 + Z + 0.26\ln[Z])},$$

and

$$\ln\Lambda_{ei} = \max\left\{1, \ln\left[\frac{3}{2e^3}\right.\right.$$

$$\times \left(\frac{A}{Z} \frac{k^3 T_e^3}{\pi N_A \rho}\right)^{1/2} \frac{1}{[Z + (1/2\alpha c)(3kT_e/m_e)^{1/2}]}\right]\right\},$$

(B5a)

$$\ln \Lambda_i = \max\left\{1, \ln\left[\frac{3}{2e^3 Z^2}\right.\right.$$

$$\times \left.\left.\left(\frac{A}{Z} \frac{k^3 T_i^3}{\pi N_A \rho}\right)^{1/2} \frac{1}{(Z + T_i/T_e)^{1/2}}\right]\right\}.$$

(B5b)

In these expressions, N_A is Avagadro's number. The ratio Z/A is 0.4 and 0.47 for fully ionized DT and LiDT, respectively. With partial ionization, we use an "effective Z" from the equation of state tables. Also, k is the Boltzmann constant and $\alpha = e^2/\hbar c$, the fine structure constant. The factors $\varepsilon \delta_T$ provide thermoelectric and electron–electron collision corrections to the electron conductivity. The argument Λ_{ei} is the harmonic mean of the classical and quantum results.[7] In addition,

$$A_{er} = C_{ve}(\nu_b + \nu_c),$$

$$\nu_b = \frac{32}{3}\left(\frac{2}{\pi m_e}\right)^{1/2} \frac{e^4 N_A^2}{\hbar c} k\left(\frac{Z^2}{A^2}\right)\frac{\rho Z}{(kT_e)^{1/2}} G(T_r/T_e), \quad \text{(B6a)}$$

with

$$G(\gamma) = \int_0^\infty \frac{d\xi\, f(\xi)[1 - e^{-\xi(1/\gamma - 1)}]}{(\gamma - 1)(1 - e^{-\xi/\gamma})}, \quad \text{(B6b)}$$

containing $f(\xi) = \int_\xi^\infty \ln\left(\sqrt{x} + \sqrt{x + 1}\right)e^{-tx}dx$, the bremsstrahlung emission spectrum. A simplified fit to $G(\gamma)$ is used in the calculations; for $\gamma \equiv T_r/T_e \to 0$, $G(\gamma) \to 1$, making ν_b the pure bremsstrahlung rate; for $\gamma \to \infty$, $G(\gamma) \to \pi^2/4$, giving pure inverse bremsstrahlung. Also,

$$\nu_c = \frac{128}{3} \frac{\pi e^2 \sigma}{(m_e c^2)^2} N_A\left(\frac{Z}{A}\right)T_r^4 k \quad \text{(B6c)}$$

is the Compton scattering rate in our radiation diffusion model; here, σ is the Stephan–Boltzmann constant. Equations [B6(a)-(c)] are due to Hurwitz.[20] Finally, we note that the radiative conductivity

$$K_r = \frac{16\sigma\lambda_R}{3} T_r^3 = \frac{16\sigma}{3\rho K_R} T_r^3, \quad \text{(B7)}$$

in which λ_R, the Rosseland mean free path, has the λ_p dependence of Eq. (5), when inverse bremsstrahlung dominates. In the calculations K_R, the Rosseland mean opacity, is obtained from tables, calculated to include the effects of bound-free transitions, bremsstrahlung and collision absorption, Compton scattering, and line absorption.

The competing thermonuclear reaction rates obey

$$\frac{\partial N_D}{\partial t} = -N_D^2\left(\overline{\sigma v}\right)_{DD} - N_D N_T\left(\overline{\sigma v}\right)_{DT},$$

(B8)

$$\frac{\partial N_T}{\partial t} = -N_D N_T\left(\overline{\sigma v}\right)_{DT} + 0.25 N_D^2\left(\overline{\sigma v}\right)_{DD}.$$

Analytic fits to Tuck's[10] Maxwell averaged cross sections $(\overline{\sigma v})$ were used for the computations. In general, the DD reactions contributed less than 1% of the energy release in our runs. For the appended LiDT results, the energy released and absorbed in n-Li reactions was also calculated.

The α particles and neutrons are transported in accordance with the Boltzmann equation, solved by the S_n method of Carlson[13] with n typically 2 for α's and 4 for neutrons. Details of the α-particle energy deposition scheme are given in Sec. III A. The energy from neutron scattering is given to the background ions. In n-Li reactions, the energy exchange is local by a prescription similar to Eq. (4). The deposited energy enters the ion and electron fields through the $\dot{S}_{i,e}$ specific energy source rate terms in Eqs. [B2(a)-(c)].

In differencing the hydrodynamics and energy equations, typically 40 to 100 zones were used with r and u assigned to the zone boundaries (j), and intensive properties, e.g., ρ and T, assigned to zone centers ($j + 1/2$). The artificial viscosity used is

$$q_{j+1/2} = \begin{cases} 2\rho_{j+1/2}(u_{j+1} - u_j)^2, & \dot{v} < 0 \text{ (compression)}, \\ 0, & \dot{v} > 0 \text{ (expansion)}. \end{cases}$$

(B9)

The energy difference equations are solved by implicit Gauss–Seidel iteration as outlined in Richtmeyer (Ref. 14, ch. 8 and 9). The time step used was the minimum of Δt values required by the Courant condition, $\Delta v/v$ and $\Delta T/T$ limits. Typically, 3500 calculational cycles were required per run. In a cycle, given the pressures, we advance the hydrodynamics and calculate the energy generated from burn, its transport and deposition. The energy equations are then iterated to solutions for the new temperatures, from which the new pressures are determined, in preparation for the next cycle.

II. Nonequilibrium code

The second, nonequilibrium code, used to cross check our results, has the same Lagrangian hydrodynamics, and ion and electron energy transport treatments, as above [Eq. (B1)], and [Eqs. (B2a,b)]. However, the term coupling the electrons to the radiation field, $A_{er}(T_e - T_r)$ in Eq. (B2b), is modified, and the transport of radiation, neutrons and fast reaction products is accomplished by Monte Carlo simulation.

The application of standard Monte Carlo schemes to radiation transport is highly inefficient in high opacity regions where photons have a high probability of absorption close to their point of origin. Our code employs "a reduced source technique," which greatly improves the efficiency of particle simulation. The full radiation transport equation is

$$\left(\frac{1}{c}\frac{\partial}{\partial t} + \Omega \cdot \nabla + \frac{1}{\lambda_a} + \frac{1}{\lambda_s}\right)\phi(\nu, \Omega)$$

$$- \int A(\nu', \Omega' \to \nu, \Omega)\phi(\nu', \Omega')\,d\nu'\,d\Omega'$$

$$\equiv L(\phi) = S(\nu) = (1/\lambda_a)B(\nu), \qquad (B10)$$

in which c is the speed of light, Ω is a unit vector in the direction of the photon transported, $d\Omega$ is the differential solid angle around this direction, and ϕ is the radiation intensity (energy/time-area-frequency). The function $S(\nu)$ is the frequency (ν) dependent emission source. In fully ionized regimes, this is bremsstrahlung, which has the nonrelativistic form

$$S(\nu) = \frac{4}{3\pi}\left(\frac{2}{\pi m_e k T_e}\right)^{1/2}\frac{\overline{Z n_i^2}\,\overline{Z^2}e^4}{\hbar c}K_0\left(\frac{h\nu}{2kT_e}\right)h$$

$$\times \exp\left(-h\nu/KT_e\right) \text{ (en/time-volume-freq-steradian)},$$
$$(B11)$$

and $B(\nu)$ is the Planckian distribution

$$B(\nu) = \frac{2h\nu^3}{c^2}\frac{1}{(\exp(h\nu/kT_e)-1)}, \qquad (B12)$$

which together define the absorption mean free path, corrected for stimulated emission λ_a. Scattering is represented by the differential inverse Compton scattering length $A(\nu,\Omega \rightarrow \nu',\Omega')$, which is given analytically in Ref. 21. A first-order relativistic approximation to the total Compton scattering length[21] is

$$\frac{1}{\lambda_s} \equiv \int A(\nu,\Omega \rightarrow \nu',\Omega')\,d\nu'\,d\Omega'$$

$$\simeq \frac{8\pi}{3}\overline{Z n_i}\,r_0^2\left[1 - \frac{2h\nu}{mc^2}\left(\frac{K_1(\xi)}{K_2(\xi)} + \frac{4}{\xi}\right)\right], \quad (B13)$$

containing r_0, the classical electron radius, and $\xi = mc^2/kT_e$. The K's are Bessel functions of the indicated order. The effects of material motion in Eq. (B10) are neglected, so the source and cross sections are isotropic.

To establish a "reduced source", we note that the left-hand side of Eq. (B10) is a linear operator acting on ϕ. Thus, if ϕ_e is an approximation to the true solution ϕ, then the deviation $\delta = \phi - \phi_e$ from the estimate obeys

$$L(\delta) = L(\phi) - L(\phi_e) = S - L(\phi_e) \equiv S_R, \quad (B14)$$

which is Eq. (B10), with $S(\nu)$ replaced by the reduced source S_R. Our procedure is to find a suitable estimated intensity ϕ_e by straightforward means, and then to solve for the intensity derivation δ by Monte Carlo simulation. Since the number of Monte Carlo "particles", required for an accurate simulation, is proportional to the square of the source intensity, considerable computation time can be saved by the transport of δ, in lieu of ϕ, if ϕ_e is good enough so $\delta \ll \phi_e \simeq \phi$ and $S_R \ll S$.

The estimate ϕ_e is found by replacing the kernel in Eq. (B10) by an isotropic kernel that produces no frequency change (i.e., coherent scattering); $A(\nu,\Omega \rightarrow \nu',\Omega') \rightarrow \delta(\nu - \nu')/4\pi\lambda_s$. This gives, for each frequency, an equation of the form

$$\left(\frac{1}{c}\frac{\partial}{\partial t} + \mu\frac{\partial}{\partial r} + \frac{(1-\mu^2)}{r}\frac{\partial}{\partial\mu} + \frac{1}{\lambda_a} + \frac{1}{\lambda_s}\right)\phi_e$$

$$- \frac{1}{2\lambda_s}\int_{-1}^{+1}\phi_e(\mu')\,d\mu' = S(\nu) = \frac{1}{\lambda_a}B(\nu), \quad (B15)$$

which is reduced to spherical coordinates. The variable $\mu = \cos\theta$, where θ is the angle between the radius vector from the center of the pellet to a photon and the velocity vector of the photon. This equation is solved by the "spherical harmonic" method (Ref. 14, chaps. 8 and 9), with truncation after the first Legendre polynomial, i.e., with a "P_1 approximation". That is, the angular dependence is approximated by

$$\phi_e = \phi_0 + \phi_1\mu. \qquad (B16)$$

Equations for ϕ_0 and ϕ_1 are obtained by taking the zeroth and first moments of Eq. (B16) over μ; thus,

$$\frac{1}{c}\frac{\partial\phi_0}{\partial t} + \frac{1}{3}\frac{\partial\phi_1}{\partial r} + \frac{2}{3}\frac{\phi_1}{r} + \frac{1}{\lambda_a}\phi_0 = \frac{1}{\lambda_a}B(\nu), \quad (B17a)$$

$$\frac{1}{c}\frac{\partial\phi_1}{\partial t} + \frac{\partial\phi_0}{\partial r} + \left(\frac{1}{\lambda_s} + \frac{1}{\lambda_a}\right)\phi_1 = 0. \qquad (B17b)$$

These equations are solved, semianalytically, for a set of frequency groups, typically thirty. For each new advancement in time, the time derivatives are replaced by their difference form, e.g.,

$$\frac{\partial\phi_0}{\partial t} \rightarrow \frac{\phi_0^{n+1} - \phi_0^n}{\Delta t_n}, \quad \phi_0^n$$

is known, the remaining terms are associated with the $n+1$ time level, and the exact ϕ_0^{n+1}, ϕ_1^{n+1} are found analytically across each zone, assuming constant λ_s, λ_a, and $B(\nu)$ within a zone. This relates the ϕ's at the zone boundaries, leading to exact solutions at these boundaries, by the inversion of a quadiagonal matrix. With ϕ_e thus determined, the reduced source $S_R(\nu)$ for each frequency group is simply

$$S_R(\nu) = (1 - 3\mu^2)\left(\frac{1}{\lambda_a}[B(\nu) - \phi_0] - \frac{\phi_1}{r} - \frac{1}{c}\frac{\partial\phi_0}{\partial t}\right),$$

$$- \frac{\phi_0}{\lambda_s} + \int \phi_0(\nu')a_0(\nu',\nu)\,d\nu'$$

$$+ \mu\int \phi_1(\nu')a_1(\nu',\nu)\,d\nu', \qquad (B18)$$

where

$$a_0(\nu',\nu) = \int A(\nu',\Omega' \rightarrow \nu,\Omega)\,d\Omega',$$

and

$$a_1(\nu',\nu) = \int A(\nu',\Omega' \rightarrow \nu,\Omega)\cos(\Omega \cdot \Omega')\,d\Omega'.$$

For Thompson scattering, $a_1 \rightarrow 0$ and $a_0 \rightarrow \delta(\nu - \nu')/\lambda_s$, so the lower line in Eq. (B18) cancels. In high opacity regions, i.e., where $l/\lambda_a \ll 1$ (with l the characteristic length of flow gradients), absorption dominates scattering, the radiation is nearly isotropic ($\phi_1 \ll \phi_0$), and slowly varying $[\partial\phi_0/\partial t \ll (c/\lambda_a)\phi_0]$, so $S_R(\nu) \rightarrow [(1 - \mu^2)/\lambda_a][B(\nu) - \phi_0]$. Furthermore, by Eq. (B17a,b), $\phi_0 \rightarrow B(\nu)$, so, indeed $S_R \ll S$, and $\delta \ll \phi_e$. In our $\rho = 3000$ g/cm³, $T = 3$ keV DT burn calculation, for example, $S_R/S \approx 0.1$, allowing 10^2 fewer Monte Carlo particles for an accurate simulation.

Given that the solution $\phi(\equiv \phi_e + \delta)$ to Eq. (B10) is

488   Phys. Fluids, Vol. 17, No. 2, February 1974

Fraley et al.   488

obtained by the above methods, there is energy exchange with the electron field such that in Eq. (B2b) the replacement

$$A_{er}(T_r - T_e) \rightarrow \frac{1}{\rho} \int \left(\frac{\phi - B(\nu)}{\lambda_a} + C(\nu)\phi \right) d\nu d\Omega, \quad (B19)$$

should be made. Here

$$C(\nu) \equiv \int_0^\infty \frac{a_0(\nu, \nu')(\nu - \nu')}{\nu} d\nu'.$$

The first term in Eq. (B19) is the bremsstrahlung exchange; the second is the Compton energy transfer. At each time step $t = t^{n+1}$, Eqs. (B2a,b) and Eq. (B17a,b) are solved together implicitly, but with $\delta = \delta^n$ assumed, for T_e^{n+1}, T_i^{n+1}, and ϕ_e^{n+1}; then, δ^{n+1} is determined explicitly by the Monte Carlo scheme.

With regard to the transport of the fast products from nuclear reactions, we note that scatterings are treated stochastically. Fast ion deposition into the field ions and electrons follows the Sec. IIIA prescription. The original fast particle sources are the D–D and D–T thermonuclear reactions. Additional fast particles are created by nuclear scatterings and "in-flight" reactions with field ions.

1. J. S. Clarke, H. N. Fisher, and R. J. Mason, Bull. Am. Phys. Soc. 17, 1035 (1972); Phys. Rev. Lett. 30, 89 (1973); 30, 249 (1973).

2. J. Nuckolls, L. Wood, A. Thiessen, and G. Zimmerman, Nature (Lond.) 239, 139 (1972).
3. N. G. Basov and O. N. Krohkin, Zh. Eksp. Teor. Fiz. 46, 171 (1964) [Sov. Phys.—JEPT 19, 123 (1964)].
4. J. M. Dawson, Phys. Fluids 7, 981 (1964).
5. W. J. Fader, Phys. Fluids 11, 2200 (1968).
6. R. R. Johnson and R. B. Hall, J. Appl. Phys. 42, 1035 (1971).
7. L. Spitzer, Physics of Fully Ionized Gases (Interscience, New York, 1969), Chap.V.
8. K. Boyer, Bull. Am. Phys. Soc. 17, 1019 (1972); Aeron. and Astron. 11, 28 (1973).
9. S. Glasstone and R. H. Lovberg, Controlled Thermonuclear Reactions (Van Nostrand, Princeton, New Jersey, 1960), p. 33.
10. J. L. Tuck, Nucl. Fusion 1, 202 (1961).
11. M. S. Chu, Phys. Fluids 15, 413 (1972).
12. C. Longmire, Elementary Plasma Physics (Wiley, New York, 1967), p. 203.
13. B. G. Carlson, Los Alamos Scientific Laboratory Report No. LA-1599 (1953).
14. R. D. Richtmeyer and K. W. Morton, Difference Methods for Initial Value Problems (Wiley, New York, 1967).
15. Y. B. Zeldovich and Y. B. Raizer, Physics of Shock Waves and High Temperature Hydrodynamic Phenomena (Academic, New York, 1966), Vol. 1, p. 218.
16. H. N. Fisher, E. J. Linnebur, R. J. Mason, and R. L. Morse, Bull. Am. Phys. Soc. 18, 683 (1973).
17. A. L. Fuller and R. A. Gross, Phys. Fluids 11, 534 (1968).
18. A. F. Nastoyashchii and L. P. Shevehenko, At. Energ. 32, 451 (1972) [Sov. J. At. Energy 32, 533 (1972)].
19. D. J. Hughes and R. B. Schwartz, Brookhaven National Laboratory Report No. 325, 2nd ed., 1958.
20. H. Hurwitz (private communication).
21. G. S. Fraley, Los Alamos Scientific Laboratory Report No. LA-4592, 1971.